Inorganic Chemistry

pubs.acs.org/IC

Article

Evolution of Bonding and Magnetism *via* Changes in Valence Electron Count in $CuFe_{2-x}Co_xGe_2$

Zachary P. Tener, Vincent Yannello, V. Ovidiu Garlea, Saul H. Lapidus, Philip Yox, Kirill Kovnir, Sebastian A. Stoian,* and Michael Shatruk*

Cite This: *Inorg. Chem.* 2022, 61, 4257–4269

Read Online

ACCESS | Metrics & More | Article Recommendations | Supporting Information

ABSTRACT: A series of solid solutions, $CuFe_{2-x}Co_xGe_2$ (x = 0, 0.2, 0.4, 0.8, and 1.0), have been synthesized by arc-melting and characterized by powder X-ray and neutron diffraction, magnetic measurements, Mössbauer spectroscopy, and electronic band structure calculations. All compounds crystallize in the $CuFe_2Ge_2$ structure type, which can be considered as a three-dimensional framework built of fused MGe_6 octahedra and MGe_5 trigonal bipyramids (M = Fe and Co), with channels filled by rows of Cu atoms. As the Co content (x) increases, the unit cell volume decreases in an anisotropic fashion: the b and c lattice parameters decrease while the a parameter increases. The changes in all the parameters are nearly linear, thus following Vegard's law. $CuFe_2Ge_2$ exhibits two successive antiferromagnetic (AFM) orderings, corresponding to the formation of a commensurate AFM structure, followed by an incommensurate AFM structure observed at lower temperatures. As the Co content increases, the AFM ordering temperature (T_N) gradually decreases, and only one AFM transition is observed for $x \geq 0.2$. The magnetic behavior of unsubstituted $CuFe_2Ge_2$ was found to be sensitive to the preparation method. The temperature-dependent zero-field ^{57}Fe Mössbauer spectra reveal two hyperfine split components that evolve in agreement with the two consecutive AFM orderings observed in magnetic measurements. In contrast, the field-dependent spectra obtained for fields ≥2 T reveal a parallel arrangement of the moments associated with the two crystallographically unique metal sites. Electronic band structure calculations and chemical bonding analysis reveal a mix of strong M−M antibonding and non-bonding states at the Fermi level, in support of the overall AFM ordering observed in zero field. The substitution of Co for Fe reduces the population of the M−M antibonding states and the overall density of states at the Fermi level, thus suppressing the T_N value.

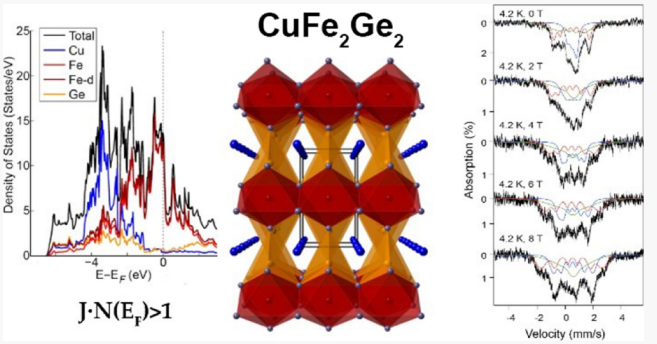

INTRODUCTION

The discovery of unconventional high-temperature superconductivity in electron- or hole-doped LaOFeAs[1,2] and $BaFe_2As_2$[3−5] spurred extensive research on related ternary systems. These efforts aim to uncover other materials that might exhibit the evolution from itinerant magnetism to superconductivity with the change in the valence electron concentration, which impacts the density of states (DOS) at the Fermi level (E_F). For example, some recent works have demonstrated that under specific doping conditions, $LaOBiS_2$,[6] $LaCo_2B_2$,[7] and YFe_2Ge_2[8] exhibit superconducting transitions at temperatures up to 10 K, which nevertheless are not as high as those found for the FeAs-based systems (up to 56 K).[9,10]

Following on the discovery of superconductivity in YFe_2Ge_2,[8] Shanavas and Singh performed a theoretical investigation of $CuFe_2Ge_2$,[11] a material with a similar composition but a drastically different structure, and predicted it to be an antiferromagnetic (AFM) metal. A follow-up experimental study[12] confirmed that $CuFe_2Ge_2$ exhibits the AFM ground state that is easily perturbed by the applied magnetic field, resulting in at least two successive magnetic transitions as a function of temperature. More recently, ^{57}Fe Mössbauer spectroscopy of this material[13] has revealed the presence of two distinctly different Fe components below the magnetic ordering temperature. One spectral component exhibits a sizable magnetic hyperfine splitting, while the other is non-magnetic and shows only a quadrupole doublet. The observation of two components in the Mössbauer spectrum correlates well with the presence of two unique Fe sites in the structure of $CuFe_2Ge_2$, but it is puzzling why only one of these components exhibits a spontaneous magnetic

Received: September 25, 2021
Published: February 28, 2022

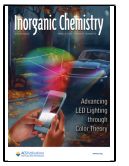

hyperfine splitting in the magnetically ordered state. Nevertheless, the unusually large line widths of the "non-magnetic" doublet observed by Bud'ko *et al.*[13] at 4.2 K might indicate a more complicated situation.

Earlier works on correlating the band structure of itinerant magnets to their magnetic properties have established that the occurrence and the nature of magnetic ordering depend not only on the DOS but also on the characteristic of the orbital overlap between the magnetic atoms.[14,15] In this vein, the type of magnetic ordering or the lack thereof can be frequently justified by the crystal orbital Hamilton population (COHP) analysis.[16] We decided to carry out a combined experimental and theoretical study to explore the correlations between the crystal and electronic structures of $CuFe_2Ge_2$ and its magnetic behavior. In particular, we would like to understand how changes in chemical bonding, triggered by the variation of the valence electron concentration (electron doping), influence the magnetic behavior of $CuFe_{2-x}Co_xGe_2$, as it is known that chemical bonding exhibits strong correlations with the nature of magnetic ordering in itinerant (metallic) magnets.[17,18] Furthermore, we set out to perform a more detailed Mössbauer investigation of these materials and, in particular, evaluate the Mössbauer spectra of $CuFe_2Ge_2$ in applied magnetic fields, which was shown to perturb the magnetic structure of this material.[12] Herein, we report a detailed investigation of the $CuFe_{2-x}Co_xGe_2$ series by means of structural, magnetic, and theoretical methods. We also describe an alternative synthesis of $CuFe_2Ge_2$ and consider in detail the correlation between magnetic properties and the electronic structure of this material. Magnetic measurements reveal synthesis-dependent magnetic behavior, while Mössbauer spectroscopy, acting as a local probe of magnetic ordering effects, reveals subtle differences in the magnetic ordering at crystallographically distinct Fe sites and a change in the nature of magnetic ordering under applied magnetic field above 2.0 T. We demonstrate that these experimental findings are in excellent agreement with the theoretical analysis of the crystal orbital overlaps in the corresponding crystal structures.

MATERIALS AND METHODS

Synthesis. All manipulations during sample preparation were carried out in an argon-filled dry box (content of O_2 < 0.1 ppm). Powders of copper (99.9%), iron (99.9%), cobalt (99.99%), and germanium (99.999%) were obtained from Alfa Aesar. Fe and Co metals were additionally purified by heating in a flow of H_2 gas for 5 h at 500 K. The other materials were used as received. Fused silica tubes were obtained from National Scientific Corporation, Inc. (Quakertown, PA).

The synthetic procedure followed the previously reported synthesis of $CuFe_2Ge_2$.[19] Samples $CuFe_{2-x}Co_xGe_2$ (x = 0, 0.2, 0.4, 0.8, and 1.0) were prepared by arc-melting pelletized stoichiometric mixtures of elements. The obtained ingots were sealed under vacuum ($<10^{-4}$ mbar) in a 10 mm inner diameter (i.d.) silica ampoules and annealed at 600 °C for 10 days, after which the samples were slowly cooled to room temperature (r.t.) by switching off the furnace.

Additionally, an alternative synthetic method was developed for $CuFe_2Ge_2$. A stoichiometric mixture of elements was sealed under vacuum in a 14 mm i.d. silica ampoule. The ampoule was heated to 1000 °C in 4 h, held at that temperature for 4 h, cooled to 600 °C in 4 h, and held at that temperature for 1 week. Finally, the sample was cooled to r.t. by switching off the furnace.

Powder X-ray Diffraction. Powder X-ray diffraction (PXRD) was carried out at r.t. on a PANalytical X'Pert Pro diffractometer with an X'Celerator detector and a Cu Kα radiation source (λ = 1.54187 Å). Each pattern was recorded in the 2θ range of 10−80° with a step of 0.017° and a total collection time of 1 h. The analysis of PXRD patterns was carried out with the HighScore Plus software.[20] To obtain accurate structural parameters for $CuFeCoGe_2$, high-resolution PXRD measurements on a sample with x = 1.0 were performed at r.t. on beamline 11-BM-B (λ = 0.414582 Å) of the Advanced Photon Source (APS) facility at Argonne National Laboratory. The unit cell parameters and the atomic coordinates established by the Rietveld refinement with FullProf[21] (Figure S1 and Table S1) were used for theoretical modeling of the electronic structure of $CuFeCoGe_2$.

Temperature-dependent PXRD measurements were performed at the APS beamline 17-BM (λ = 0.24153 Å) to study the thermal stability of $CuFe_2Ge_2$. The sample was held in an evacuated and sealed 0.5 i.d. silica glass capillary. The capillary was loaded into a flow cell[22] and centered in the X-ray beam. The PXRD patterns were collected at multiple temperatures between 400 and 1000 °C to evaluate the temperature-dependent structural behavior of the sample.

Physical Measurements. The elemental analyses were performed on an FEI Nova 400 Nano scanning electron microscope equipped with an energy-dispersive X-ray (EDX) spectrometer. Multiple locations on pelletized polycrystalline samples were probed to establish the statistically averaged composition of each sample. Magnetic data were collected using a magnetic property measurement system (MPMS-XL, Quantum Design) equipped with a superconducting quantum interference device. Direct current magnetic susceptibility was measured in the zero-field-cooled (ZFC) and field-cooled (FC) modes in the 1.8−300 K temperature range, with applied fields of 10, 100, 1000, and 10 000 Oe.

Mössbauer Spectroscopy. Absorbers characterized in this study consisted of ∼20 mg finely ground powder dispersed in eicosane, which functioned as an inert matrix. The spectra were recorded using a spectrometer operated in a constant acceleration mode, equipped with a Super VariTemp Janis cryostat, and an 8 T American Magnetics superconducting magnet. The γ-ray source consisted of ∼100 mCi ^{57}Co dispersed in a Rh metal foil. For the field-dependent spectra, the magnetic field was applied parallel to the propagation direction of the γ-radiation. Isomer shifts are quoted against the center of a r.t. spectrum recorded for an α-Fe foil.

Spectral simulations were performed using the WMOSS software (see Co., formerly WEB Research Co., Edina, MN). Voigt-based model, developed by Rancourt and Ping,[23] was used to describe the arbitrary hyperfine field distribution (HFD). In this model, a general HFD is described by considering a sum of elemental Gaussian components, each of which is characterized by three distinct parameters: a weight factor, p (%), the center, z (T), and the full width at half-maximum (FWHM), dz (T), of the respective Gaussian distribution. Assuming that all Fe sites exhibit identical f-recoilless fractions, p can be used to determine the amount of Fe accounted for by the respective component. In addition to these parameters, each elemental sextet used to construct an individual Gaussian HFD is characterized by the following: (i) Γ—the FWHM of the intrinsic Lorentzian line shape, (ii) ε—the electric field gradient (EFG) tensor component along the internal field, (iii) δ—the isomer shift, and (iv) h_1/h_3 and (v) h_2/h_3—the intensity ratios of the outer (1, 6) lines to the inner (3, 4) lines and of the middle (2, 5) lines to the inner (3, 4) lines, respectively. In addition to using the HFD model, simulations were also performed considering a magnetically uniaxial Kramers doublet, that is, an effective S = 1/2 with g_z = 2.0 and $g_x = g_y$ = 0, and a slow relaxation regime of the electronic spin. In this case, the magnitude of the magnetic hyperfine splitting was set using a hyperfine coupling constant (A_z), which is related to the internal field (B_{int}) as $A_z = 2B_{int}$. Furthermore, the magnitude of the EFG tensor along the direction of the internal field was set using an appropriate, non-standard EFG asymmetry parameter, $-100 < \eta < 100$, and the ΔE_Q value determined above the ordering temperature. Using this model, the distribution of hyperfine fields was evaluated using an effective line width, which was contrasted with that observed for the paramagnetic states.

The hyperfine splitting of a Mössbauer spectrum recorded for a selected Fe-containing species is determined by the contributions of the nuclear Zeeman and quadrupolar interactions. In the zero field,

https://doi.org/10.1021/acs.inorgchem.1c02997
Inorg. Chem. 2022, 61, 4257−4269

only the quadrupole interaction is effective and a two-line spectrum (a quadrupole doublet) is observed. Under the non-zero applied field, when the nuclear Zeeman interaction is dominant, we observe either a six-line spectrum for species with uniaxial magnetic properties, such as those exhibiting an easy axis of magnetization, or a four-line spectrum for magnetically isotropic sites.

Neutron Powder Diffraction. The sample of $CuFe_2Ge_2$ prepared by conventional annealing was studied with the HB-2A high-resolution powder diffractometer housed in the High-Flux Isotope Reactor at Oak Ridge National Laboratory (ORNL). A sample of ~3 g, held in a cylindrical vanadium container, was placed in a top-loading temperature control system. Measurements were performed using λ = 1.539 and 2.41 Å monochromatic neutron beams provided by a vertically focused Ge monochromator. The data were collected by scanning the detector array consisting of 44 ^{3}He tubes to cover the total 2θ range of 7−133° in steps of 0.05°. Rietveld refinement of the collected data was carried out using FullProf.[21] An analysis of symmetry-allowed magnetic models was performed using SARAh representational analysis software[24] and MAXMAGN at the Bilbao crystallographic server.[25] Data collections were performed at selected temperatures to probe the different magnetically ordered states.

Quantum Chemical Calculations. The density functional theory (DFT) band structure calculations and interatomic crystal orbital Hamilton population (COHP) analysis[16] were performed using the tight binding-linear muffin tin orbitals-atomic sphere approximation (TB-LMTO-ASA) software package.[26] The structural parameters (unit cell dimensions and atomic coordinates) for $CuFe_2Ge_2$ and $CuCo_2Ge_2$ were taken from the reported r.t. crystal structures,[19] while the structural parameters for $CuFeCoGe_2$ were derived from the Rietveld refinement of the powder diffraction pattern (Figure S1 and Table S1). Various occupation patterns were tested, but no substantial difference in either the DOS curves or the COHP curves was observed. As such, the lowest energy structure was used for all curves shown, in which Co and Fe occupied, respectively, the Fe1 and Fe2 sites in the original structure of $CuFe_2Ge_2$. Exchange and correlation were treated using the von Barth−Hedin local density approximation.[27] The radial scalar-relativistic Dirac equation was solved self-consistently to obtain the partial waves.

Two symmetrically inequivalent empty spheres were necessary to fill the volume of the cell with spheres of overlap equal to ~8.6% for all phases, resulting in a total of 10 additional spheres per unit cell. The two symmetrically inequivalent positions were (0.25, 0, and 0.6986) and (0.9779, 0.1831, and 0.2344) for $CuFe_2Ge_2$ and (0.25, 0, and 0.6982) and (0.9772, 0.1809, and 0.2399) for $CuFeCoGe_2$. The calculations used a basis set of Cu-, Fe-, Co 4s/4p/3d, Ge 4s/4p/(4d), and empty spheres-1s/(2p)/(3d) (downfolded orbitals in parentheses).[28,29] The radii of the Wigner−Seitz spheres in $CuFe_2Ge_2$ were Cu, 2.71 Å; Fe, 2.61 and 2.56 Å; Ge, 2.81 and 2.64 Å; and empty spheres, 1.97 and 1.09 Å. For $CuFeCoGe_2$, they were Cu, 2.71 Å; Fe, 2.53 Å; Co, 2.59 Å; Ge, 2.76 and 2.61 Å; and empty spheres, 1.92 and 1.11 Å. Sets of 23 × 29 × 17 k-points in the irreducible wedge of the tetragonal Brillouin zone were used for the DOS calculations, and 13 × 17 × 10 k-points were used for the COHP analysis.

RESULTS AND DISCUSSION

Synthesis. The solid solutions $CuFe_{2-x}Co_xGe_2$ (x = 0, 0.2, 0.4, 0.8, and 1.0) were prepared by arc-melting the nominal compositions, followed by homogenizing annealing at 600 °C. Similar to the previous reports,[12,19] it was found that not exceeding this temperature during the annealing step was critical to obtaining a single-phase product. PXRD analysis revealed that all samples were phase-pure, showing a good match to the pattern calculated for the orthorhombic $CuFe_2Ge_2$ (see the Crystal Structure section).

The elemental content established for each sample by EDX analysis agreed well with the nominal composition used in the synthesis. Fitting the composition to the formula $Cu_aFe_bCo_cGe_2$ (with the Ge stoichiometric coefficient fixed at 2) resulted in the systematic observation of $a < 1$ and $b + c > 2$ (Figure 1). These deviations might indicate a slight antisite

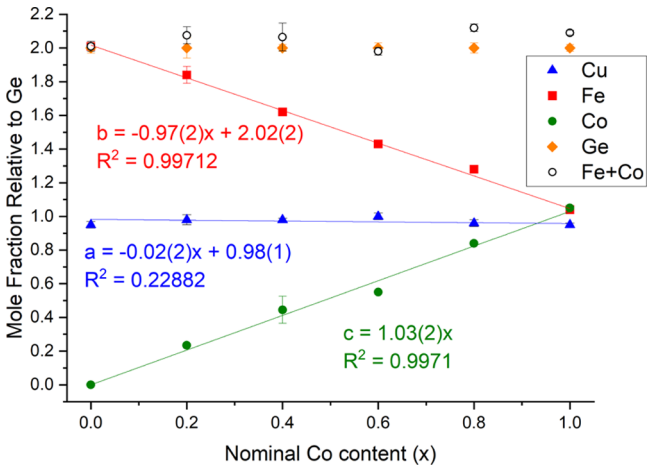

Figure 1. Elemental compositions of $CuFe_{2-x}Co_xGe_2$ samples determined by EDX spectroscopy. The compositions were calculated as $Cu_aFe_bCo_cGe_2$, with the Ge content fixed at 2.0.

disorder between the Cu and Fe/Co crystallographic positions, although we did not explore this finding further. Noteworthily, Zavalij *et al.* also observed a homogeneity range in $Cu_{1\pm y}Co_{2\pm y}Ge_2$, which they justified by Cu/Co mixing in the crystallographic sites.[19]

To study the thermal stability of $CuFe_2Ge_2$, temperature-dependent synchrotron powder diffraction was performed. Analysis of the PXRD data reveals a phase transition from the orthorhombic structure reported at r.t. (space group *Pmma*)[19] to a hexagonal structure at temperatures above 600 °C. The loss of the orthorhombic distortion can be seen from the fusion of some PXRD peaks as the temperature is increased (Figure 2a). The unit cell parameters (Figure S2) and volume (Figure 2b) calculated for the orthorhombic symmetry show a discontinuity at 655 °C, which is, therefore, assigned as the phase transition temperature. Above 950 °C, the loss of crystallinity is observed, suggesting that the sample is melting (Figure S3). Cooling the melt leads to the reversible formation of the hexagonal phase that transforms to the orthorhombic phase below 655 °C. Interestingly, it was noted by Zavalij *et al.* that the solid solutions $Cu_{1\pm y}Co_{2\pm y}Ge_2$, isostructural to $CuFe_2Ge_2$, also showed the tendency to develop hexagonal symmetry for compositions with the lower Cu content.[19]

The indication that the tertiary mix of elements can be liquefied even at temperatures below 1000 °C, along with the relatively low melting points of both Cu (1085 °C) and Ge (938 °C), suggested that raising the temperature to arc-melting levels might be avoided and the target compounds could be formed at temperatures achievable in a standard laboratory furnace. Correspondingly, samples were prepared by quickly heating a pelletized stoichiometric mixture of elements and holding it for 4 h at 1000 °C to partially melt the reactants, then cooling it to 600 °C, and maintaining at that temperature for 1 week to achieve the complete transformation to the orthorhombic phase, as discussed above. This method was found effective for the synthesis of $CuFe_2Ge_2$ (Figure S4) but showed the presence of impurities in Co-containing samples, judging by the appearance of extrinsic signals in magnetic measurements.

https://doi.org/10.1021/acs.inorgchem.1c02997
Inorg. Chem. 2022, 61, 4257−4269

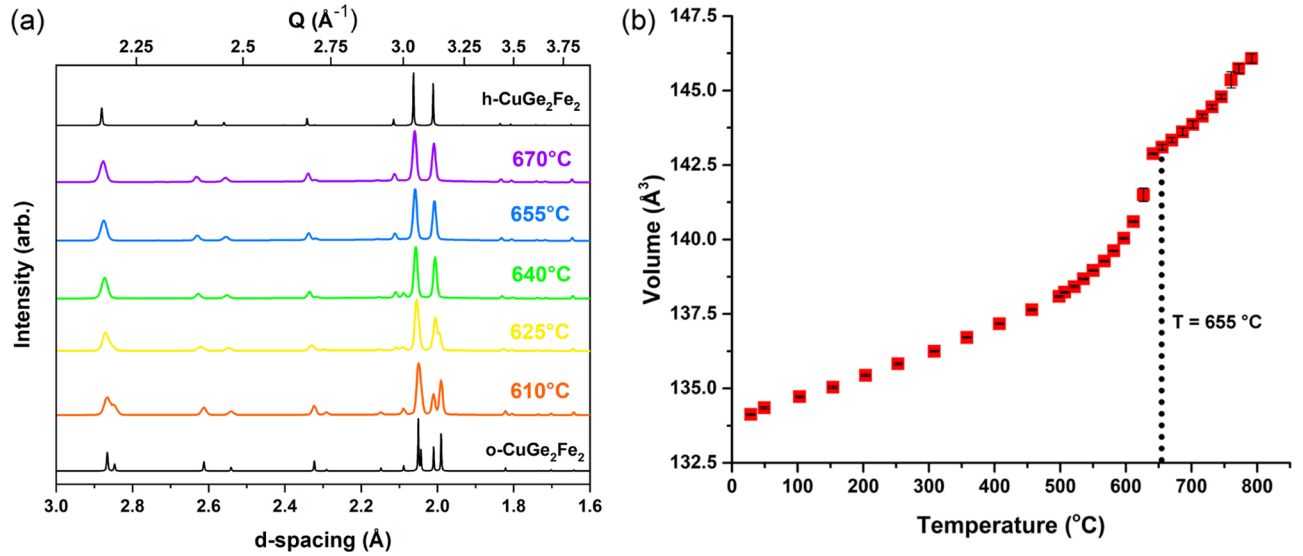

Figure 2. (a) Fragments of temperature-dependent PXRD patterns (λ = 0.24153 Å) of $CuFe_2Ge_2$ showing the transition from the low-temperature orthorhombic to the high-temperature hexagonal structure. (b) Temperature dependence of the unit cell volume calculated for the orthorhombic structure.

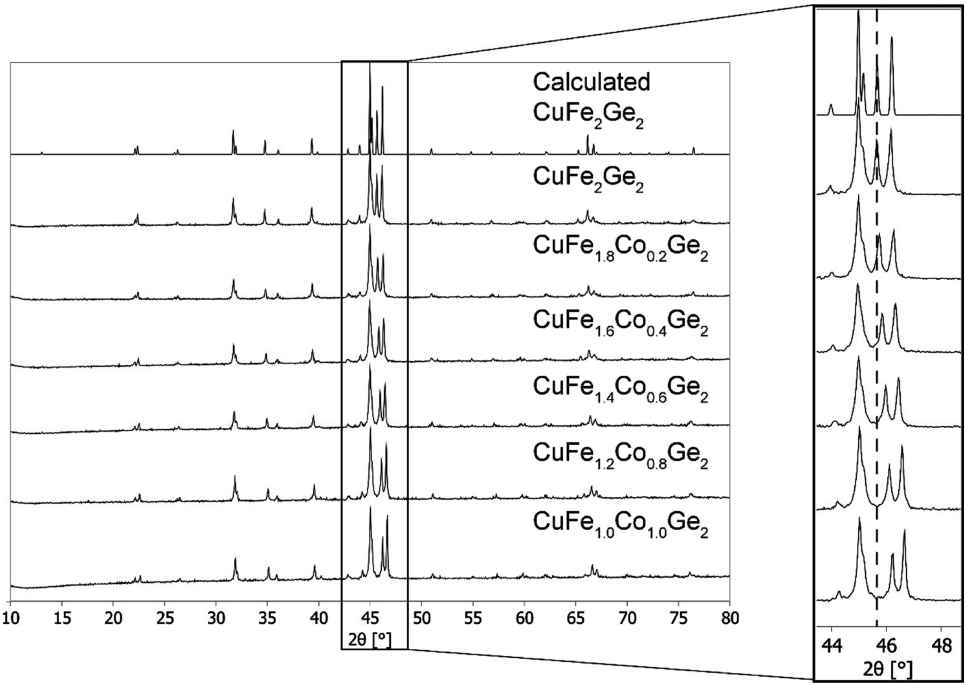

Figure 3. X-ray powder diffraction patterns of $CuFe_{2-x}Co_xGe_2$.

Crystal Structure. The analysis of PXRD data of the reaction products (Figure 3) revealed that all samples retain the original orthorhombic structure of $CuFe_2Ge_2$. The substitution of Co for Fe leads to the decrease in the unit cell volume, in agreement with the smaller size of Co atoms. The unit cell parameters and volume change almost linearly with the Co content (x), thus following Vegard's law (Figure 4 and Table 1). Such behavior can be attributed to the Fe and Co atoms sharing the same Wyckoff positions, 2d (0, 0.5, and 0.5) and 2f (0.25, 0.5, and z), with a single positional variable z. (As shown below, these changes are also reflected in the magnetic behavior of the Co-substituted samples.) One might argue that there are two linear regimes, corresponding to the low and intermediate Co content, and thus, the structural changes in the solid solution deviate from Vegard's law. This deviation, however, is likely a result of the slight deviation from the linearity in the Co content, as shown by the EDX analysis (Figure 1).

In the Rietveld refinement of the crystal structure of $CuFeCoGe_2$, we assumed equal distribution of Fe and Co atoms over the transition metal sites 2d and 2f. Such refinement, however, led to drastically different atomic displacement parameters for the Fe1/Co1 and Fe2/Co2 sites [U_{iso} = 0.0039(2) Å^2 and 0.0143(3) Å^2, respectively]. It is possible that the elemental distribution over these sites is not completely random. Besides, some mixing of Cu into these positions also cannot be completely ruled out.[19] A more accurate determination of the site occupancy model and

https://doi.org/10.1021/acs.inorgchem.1c02997
Inorg. Chem. 2022, 61, 4257−4269

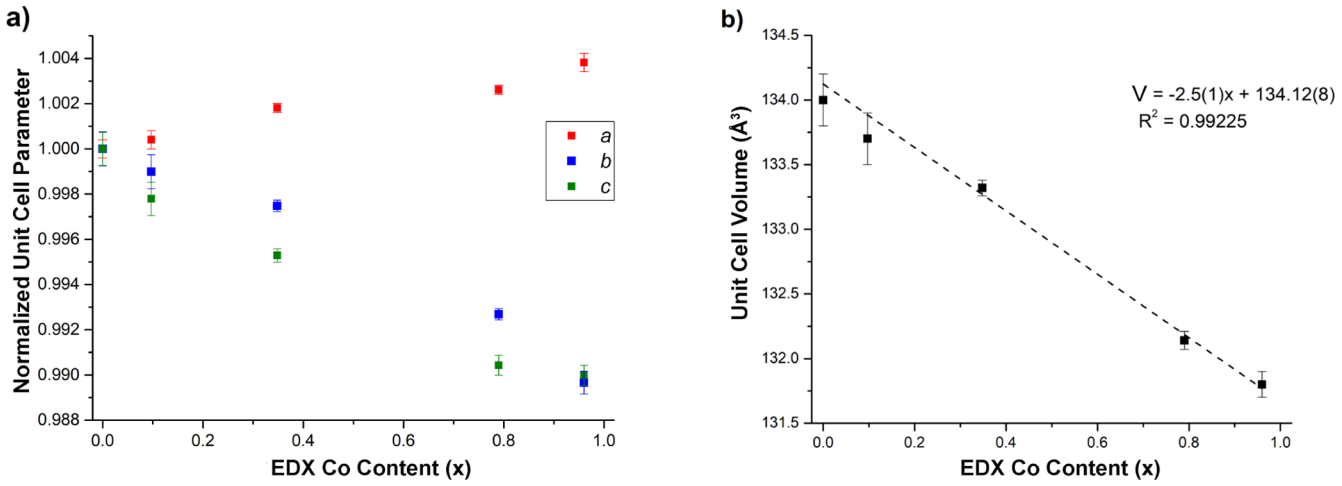

Figure 4. Unit cell parameters (a) and volume (b) for $CuFe_{2-x}Co_xGe_2$. Wherever the error bars are not visible, they are smaller than the symbol size.

Table 1. Co Content (x), Unit Cell Parameters, and Magnetic Ordering Temperatures (T_N) for $CuFe_{2-x}Co_xGe_2$

nominal composition	Co content from EDX analysis (x)	a (Å)	b (Å)	c (Å)	V (Å^3)	T_{N1} (K)	T_{N2} (K)
$CuFe_2Ge_2$[a]		4.977(2)	3.9703(8)	6.787(1)	134.11(6)	171	148
$CuFe_2Ge_2$		4.977(2)	3.966(3)	6.791(5)	134.0(2)	180	75
$CuFe_{1.8}Co_{0.2}Ge_2$	0.097(9)	4.979(2)	3.962(3)	6.776(5)	133.7(2)		56
$CuFe_{1.6}Co_{0.4}Ge_2$	0.348(9)	4.986(1)	3.956(1)	6.759(2)	133.32(6)		32
$CuFe_{1.2}Co_{0.8}Ge_2$	0.79(3)	4.990(1)	3.937(1)	6.726(3)	132.14(7)		15
$CuFeCoGe_2$	0.96(2)	4.996(2)	3.925(2)	6.723(3)	131.8(1)		8[b]

[a]This sample was obtained by conventional annealing, while the other samples were obtained by arc-melting. [b]$CuFeCoGe_2$ exhibits a spin glass transition at 8 K.

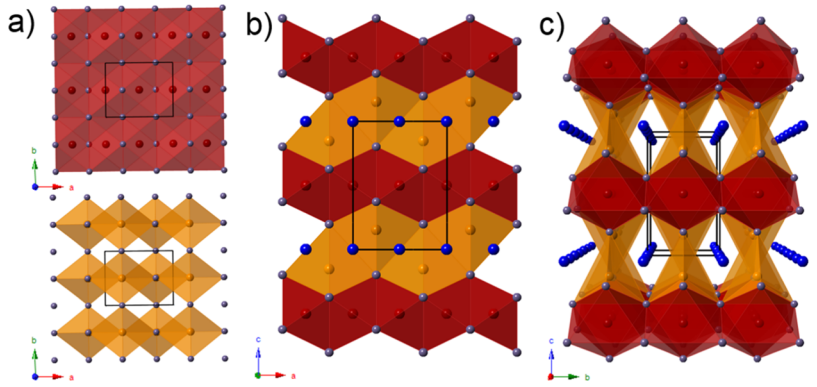

Figure 5. Crystal structure of $CuFe_2Ge_2$: (a) view of the layers of $FeGe_6$ octahedra (top) and $FeGe_5$ bipyramids (bottom) parallel to the *ab* plane. (b) Stacking of polyhedral layers along the *c*-axis. (c) Perspective view of the structure showing the channels filled with rows of Cu atoms parallel to the *a*-axis. Color scheme: Cu = blue, Fe1 = red, Fe2 = orange, Ge = gray. (The Fe1 and Fe2 sites are shown with different colors in order to facilitate the following discussion of magnetic behavior in the light of chemical bonding.)

possible antisite disorder requires neutron diffraction experiments on the $CuFeCoGe_2$ material.

While the crystal structure of $CuFe_2Ge_2$ was previously described,[19] we briefly discuss it here using an alternative, polyhedral presentation, which will be helpful for understanding the difference in unique iron environments in $CuFe_2Ge_2$ and discussing the correlation between the magnetic properties and electronic structure and bonding in this material. The crystal structure can be viewed as assembled of Fe-centered distorted polyhedra of Ge: layers of $FeGe_6$ octahedra alternate with layers of $FeGe_5$ trigonal bipyramids along the *c*-axis (Figure 5). The octahedra share faces in the *a* direction and edges in the *b* direction, while the trigonal bipyramids share edges in *a* direction and vertices in the *b* direction. Channels formed within the layers of $FeGe_5$ bipyramids are occupied by chains of Cu atoms. The underlying arrangement of the magnetic atoms can also be described as consisting of saw-tooth chains of isosceles triangles running along the *a*-axis, with Fe1 forming the base of the saw-tooth chain and Fe2 atoms defining the vertices of the triangles.

Magnetic Properties. The arc-melted sample of $CuFe_2Ge_2$ exhibits divergence between the FC and ZFC magnetization data at ~230 K in a 100 Oe applied field (black curves in Figure 6), while the sample obtained by conventional annealing shows an abrupt increase in both the

https://doi.org/10.1021/acs.inorgchem.1c02997
Inorg. Chem. 2022, 61, 4257−4269

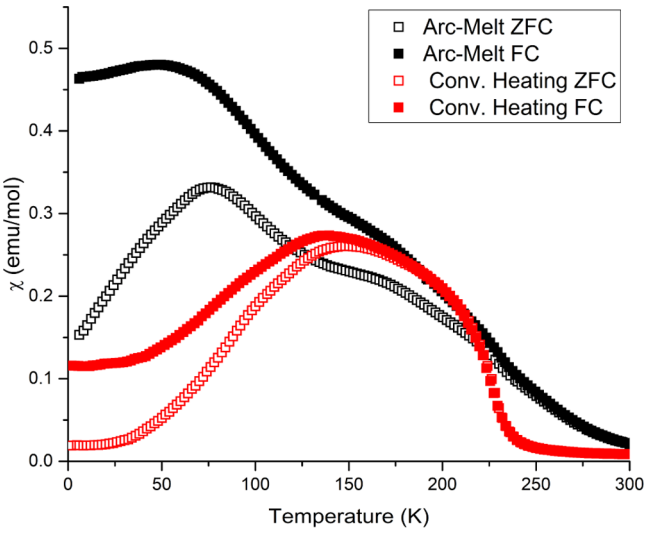

Figure 6. Temperature dependence of FC (filled symbols) and ZFC (open symbols) magnetic susceptibility for two samples of $CuFe_2Ge_2$ measured under an applied magnetic field of 100 Oe.

FC and ZFC magnetization at this temperature but without any notable divergence (red curves in Figure 6). The initial increase in magnetization also agrees with the observation made by May *et al.* on the sample they obtained by arc-melting.[12] Interestingly, and also in agreement with this earlier report, we find that the Mössbauer spectra and neutron diffraction patterns indicate that the first magnetic phase transition in this material takes place only at T_{N1} = 175 K (see below). Thus, we attribute the initial increase in FC and ZFC magnetization to some short-range effects rather than to a long-range magnetic phase transition. Such a behavior might stem from competing exchange interactions that lead to competition between different ground states. A justification for these competing interactions will be provided in a later section through the analysis of the electronic structure and bonding characteristic.

May *et al.* demonstrated that a second magnetic phase transition takes place at T_{N2} = 125 K, corresponding to the formation of an incommensurate AFM structure.[12] We also observe an increase in both FC and ZFC susceptibility around this temperature for the arc-melted sample, although the annealed sample exhibits a maximum in the FC susceptibility near 125 K, after which both the FC and ZFC susceptibility curves notably decrease. On the other hand, for the arc-melted sample, the maxima in the ZFC and FC susceptibility curves are observed at ∼75 and ∼55 K, respectively, suggesting that the lower-temperature magnetic behavior is sensitive not only to the applied magnetic field but also to the thermal history of the sample. The magnetic behavior of the annealed sample is also very sensitive to the magnitude of the applied field (Figure S5), in agreement to the observation made for the arc-melted sample in the previous report.[12]

Even a small substitution of Co for Fe leads to strong suppression of magnetization, as can be seen from the magnetic behavior of the $CuFe_{2-x}Co_xGe_2$ sample with x = 0.2 (blue curves in Figure 7a). Despite the initial increase in magnetization at ∼220 K, the divergence of the FC and ZFC data occurs only at ∼150 K, and a lower-temperature cusp in the ZFC curve suggests an AFM transition at $T_N \approx 56$ K. The sample with x = 0.4 exhibits AFM ordering at even lower temperature, with T_N = 32 K (green curves in Figure 7a). The increase in the Co content leads to further suppression of magnetization and a decrease in the AFM ordering temperature to 15 K for x = 0.8 and 8 K for x = 1 (Figure 7b).

The plateau-like characteristic of the low-temperature FC susceptibility and the cusp observed in the ZFC susceptibility suggest possible spin glassiness, especially evident in the samples with the higher Co content. To investigate such a possibility, AC magnetic susceptibility measurements were performed on the sample with x = 1.0 (Figure 8). While the data are rather noisy because of the low value of the magnetic moment, the sample exhibits an obvious shift in the temperature (T_f) of the maximum of the in-phase AC susceptibility signal (χ') as a function of the measurement frequency (f). These data were used to calculate the empirical Mydosh parameter, $\varphi = \frac{\Delta T_f}{T_f \log(\Delta f)}$, which was found equal to 0.009(1) for x = 1.0. This value falls in the expected range for spin glasses, which typically exhibit $0.004 < \varphi < 0.08$.[30]

Electronic Structure Calculations. To understand the change in the magnetic behavior as a function of Co content, we investigated the electronic structures of $CuFe_2Ge_2$, $CuFeCoGe_2$, and $CuCo_2Ge_2$ by theoretical calculations. The

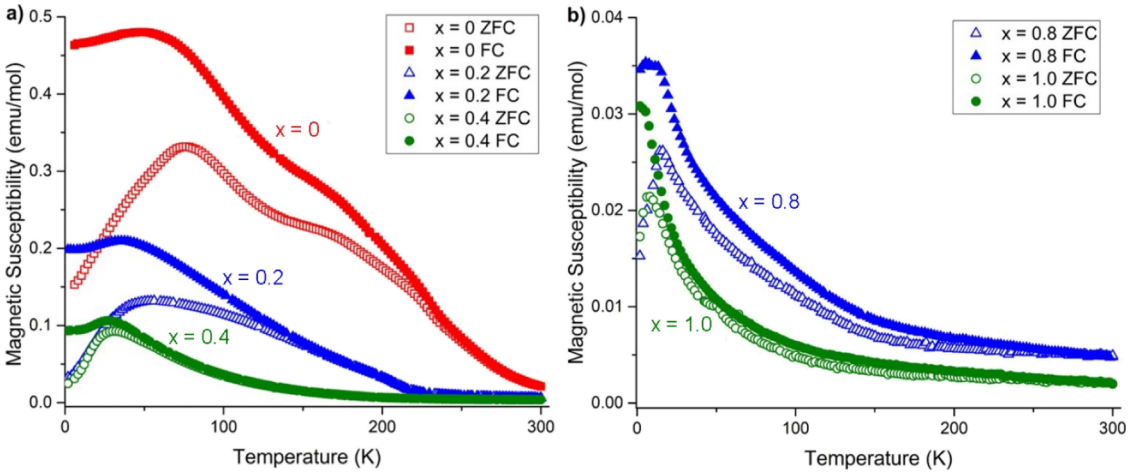

Figure 7. Temperature dependence of FC (filled symbols) and ZFC (open symbols) magnetic susceptibility for $CuFe_{2-x}Co_xGe_2$ for x = 0 (arc-melted), 0.2, and 0.4 (a), and x = 0.8 and 1.0 (b), measured under an applied field of 100 Oe.

https://doi.org/10.1021/acs.inorgchem.1c02997
Inorg. Chem. 2022, 61, 4257−4269

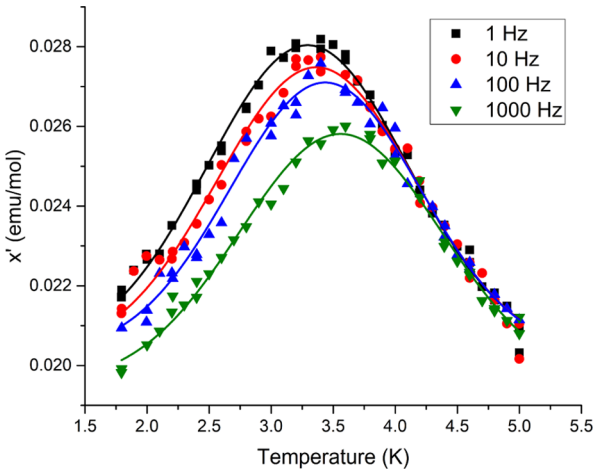

Figure 8. In-phase AC magnetic susceptibility of $CuFeCoGe_2$. The solid lines indicate the Gaussian fit performed to determine the peak maxima, which were used as $T_f(f)$ values to calculate the Mydosh parameter (φ).

DOS plots, calculated as outlined in the Materials and Methods section, appear to be very similar for all the three structures (Figure 9a), but some notable differences do exist. The DOS near the Fermi level (E_F = 0 eV) is primarily attributable to the Fe- or Co-based 3d states, with Cu- and Ge-based states dominating at lower energies. The dominant Fe and Co 3d states result in two large peaks near E_F in all compounds. In $CuFe_2Ge_2$, the Fermi level crosses the larger of these peaks; in $CuFeCoGe_2$, it falls into a pseudo-gap between the peaks, and a further increase in the valence electron count in $CuCo_2Ge_2$ leads to the Fermi level crossing a smaller DOS peak just above the pseudo-gap.

The value of DOS at E_F has been used previously to justify itinerant magnetism in $CuFe_2Ge_2$.[11] According to the Stoner criterion, itinerant magnetic ordering is favored when $J{\cdot}N(E_F) > 1$, where J is the magnetic exchange coupling constant and $N(E_F)$ is the DOS at the Fermi level.[31] The value of J can be approximated by those tabulated for elemental metals.[32] Using this approximation, the $J{\cdot}N(E_F)$ values calculated for $CuFe_2Ge_2$ and $CuFeCoGe_2$ are, respectively, 1.6 and 0.50 per transition metal atom. These values indicate that $CuFe_2Ge_2$ should exhibit magnetic ordering, while $CuFeCoGe_2$ should not, in agreement with the results of magnetic measurements that show the formation of a spin-glass state in $CuFeCoGe_2$. Based on the observed trend in the DOS plot, the $J{\cdot}N(E_F)$ product should decrease gradually upon substitution of Co for Fe, eventually falling below 1, which agrees with the suppression of itinerant magnetic ordering in $CuFe_{2-x}Co_xGe_2$ for higher values of x.

To get chemical insight into the variation of magnetic properties, we carried out crystal orbital Hamilton population (COHP) analyses. Three short M−M (M = Fe or Co) interactions exist in the system, M1−M1, M1−M2, and M2−

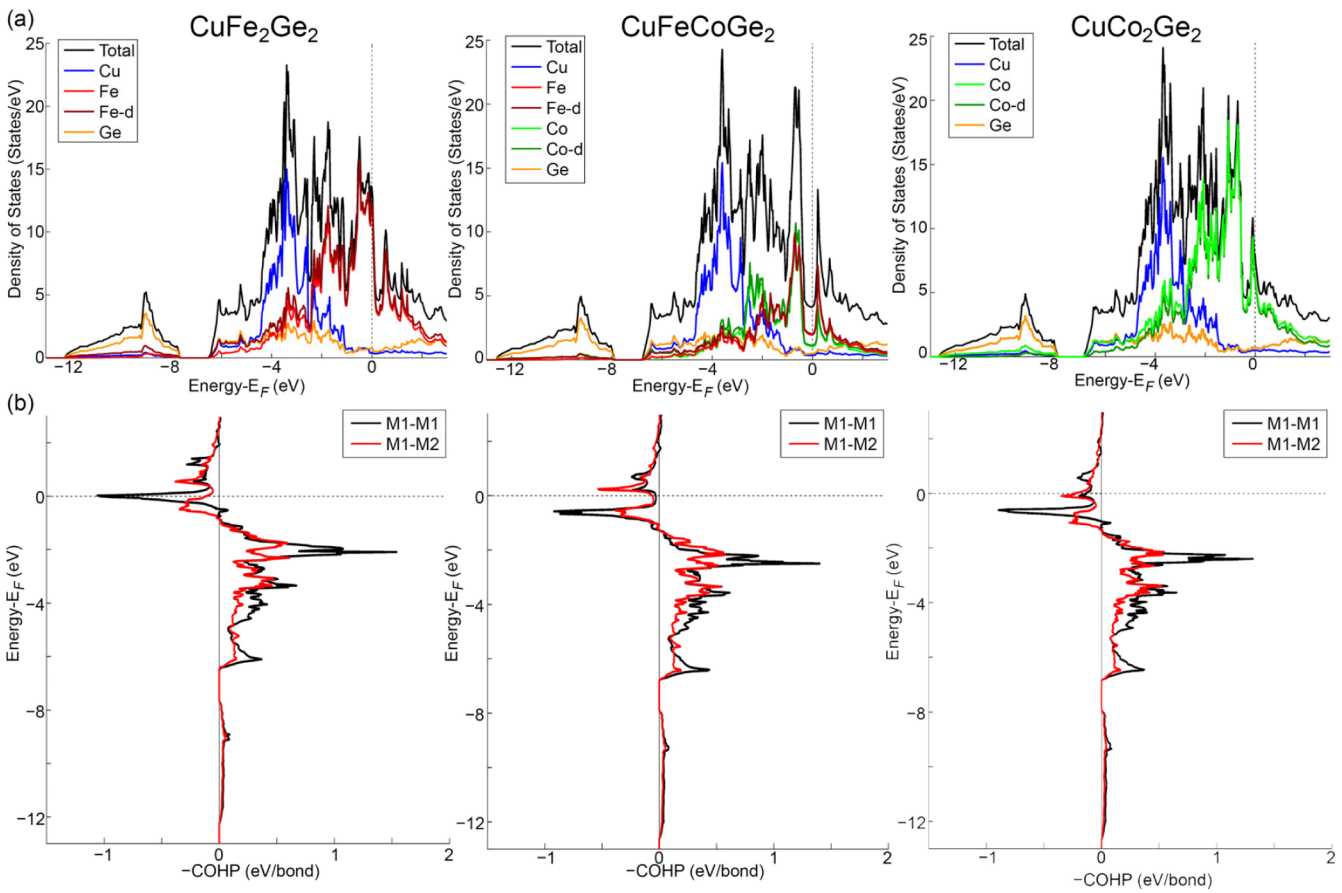

Figure 9. (a) DOS curves for $CuFe_2Ge_2$, $CuFeCoGe_2$, and $CuCo_2Ge_2$, with projected DOS shown for each element and for the transition metal 3d states. (b) −COHP curves for $CuFe_2Ge_2$, $CuFeCoGe_2$, and $CuCo_2Ge_2$ for the two important Fe/Co bonding interactions, M1−M1 and M1−M2. For $CuFe_2Ge_2$ and $CuCo_2Ge_2$, M1 = M2 = Fe or Co. For $CuFeCoGe_2$, M1 = Co and M2 = Fe.

https://doi.org/10.1021/acs.inorgchem.1c02997
Inorg. Chem. 2022, 61, 4257−4269

M2, where M1 and M2 are transition metal atoms inside the Ge octahedra and trigonal bipyramids, respectively (red and orange polyhedra in Figure 5). According to the experimentally determined crystal structures, the corresponding M−M distances are, respectively, 2.489, 2.655, and 3.248 Å in $CuFe_2Ge_2$, 2.487, 2.626, and 3.229 Å in $CuFeCoGe_2$, and 2.502, 2.631, and 3.229 Å in $CuCo_2Ge_2$. Both the M1−M1 and M1−M2 COHP curves (Figure 9b) reveal significant interactions along the *a*-axis and in the *ac* plane, respectively (Figure 10), while the M2−M2 COHP (not shown) has no interactions, in agreement with the much longer distance between the M2 atoms.

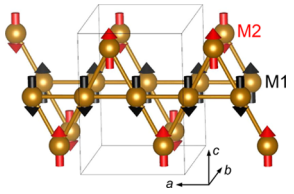

Figure 10. Magnetic structure of $CuFe_2Ge_2$, as reported by May *et al.*,[12] showing FM M1−M1 and AFM M1−M2 interactions between the magnetic sites. The adjacent layers of magnetic moments are arranged antiparallel to one another, thus creating an overall AFM structure.

Dronskowski and Landrum showed that the driving force for itinerant ferromagnetism or antiferromagnetism lies, respectively, in the local antibonding or non-bonding characteristic of states located at the Fermi level.[15] Our COHP analysis reveals that at the Fermi level of $CuFe_2Ge_2$, the M1−M1 interactions, which mainly occur along the *a*-axis, are strongly antibonding, while the M1−M2 interactions, predominantly in the *ac* plane, fall in a relatively non-bonding region (Figure 9b, left). These observations correlate with the experimental magnetic structure of $CuFe_2Ge_2$,[11] in which the M1 magnetic moments within the layers of MGe_6 octahedra couple FM to each other but AFM to the M2 moments located in the layers of MGe_5 trigonal bipyramids (Figure 10). A COHP analysis of the magnetic coupling between the M2 sites along the *c*-axis is insufficient due to the lack of direct orbital overlap, although the experimental magnetic structure suggests FM ordering along this direction.

As Co is added to the system, both M1−M1 and M1−M2 interactions at the Fermi level become nearly non-bonding for $CuFeCoGe_2$ (Figure 9b, center) and again weakly antibonding for $CuCo_2Ge_2$ (Figure 9b, right). While such interactions in $CuFeCoGe_2$ would suggest the possibility of AFM ordering, the lack of sufficiently high DOS at the Fermi level results in the suppression of itinerant magnetism in this material, in agreement with the experimental data. The observed electronic structure also suggests that $CuCo_2Ge_2$, most likely, should not exhibit magnetic ordering, but further investigation of this material is required to verify such a hypothesis.

Despite some general similarities, there are notable differences in the characteristic of the ZFC and FC magnetization curves recorded for the arc-melted and conventionally annealed samples of $CuFe_2Ge_2$. This observation raises the question whether there exists a fundamental difference in the microscopic magnetic behavior of the material prepared by different synthetic methods. To address this question, we use ^{57}Fe Mössbauer spectroscopy and neutron diffraction. Thus, the remainder of this work is dedicated to the in-depth discussion of the magnetic properties and magnetic structure of unsubstituted $CuFe_2Ge_2$.

^{57}Fe Mössbauer Spectroscopy. *Comparison of Samples Prepared by the Two Synthetic Methods.* To investigate the electronic structure of $CuFe_2Ge_2$ and to elucidate its magnetic behavior, we have collected a series of temperature- and field-dependent ^{57}Fe Mössbauer spectra for samples of $CuFe_2Ge_2$ prepared by both synthetic methods. At 200 K, both samples show similar zero-field spectra that consist of a slightly asymmetric quadrupole doublet (Figure 11). Spectral simulations, obtained considering just one spectral component, yielded nearly identical isomer shift (δ) and quadrupole splitting (ΔE_Q) values (Table 2). It should be noted that, to reproduce the experimental data, these simulations required the use of Gaussian line shape instead of Lorentzian. Additionally, the line width ($\Gamma_{L/R}$) observed for the arc-melted sample is ∼15% larger than that obtained for the sample prepared by conventional annealing. Together, these observations suggest that the observed spectra originate from a heterogeneous distribution of Fe sites and that the heterogeneity seems to slightly larger for the arc-melted sample, despite the fact that this sample was subjected to homogenizing annealing.

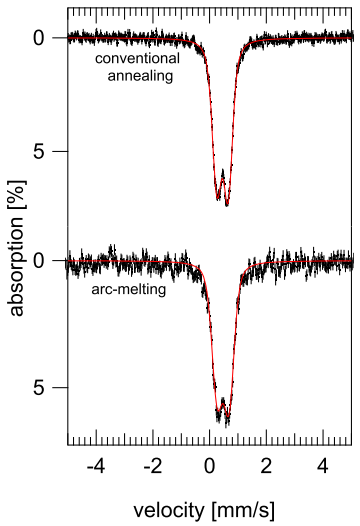

Figure 11. Zero-field ^{57}Fe Mössbauer spectra recorded at 200 K for the $CuFe_2Ge_2$ samples prepared by conventional annealing (top) and arc-melting (bottom). The solid red lines superimposed over the experimental data are simulations obtained using the values listed in Table 2.

The ^{57}Fe Mössbauer spectra recorded at 4.2 K (Figure S6) are also similar for the samples prepared by both methods. The spectra recorded under an applied field of 8 T are essentially identical, and the spectra recorded in zero field exhibit an analogous hyperfine splitting pattern, which originates from the overlap of at least two spectral components. Our analysis reveals that the relative ratio of the two spectral components changes by at most 5% between the two samples and that the relative differences in the magnetic hyperfine splitting of the analogous spectral components of either sample originate from variations in internal fields smaller than 0.1 T.

Temperature Dependence of the Zero-Field Spectra. Typically, the presence of Fe sites with different coordination environments leads to distinct quadrupole doublets in zero-field Mössbauer spectra. Consequently, the observation for

https://doi.org/10.1021/acs.inorgchem.1c02997
Inorg. Chem. 2022, 61, 4257−4269

Table 2. Mössbauer Parameters Describing the Zero-Field Spectra Recorded at 200 K

simulation method	sample preparation method	δ (mm/s)	ΔE_Q (mm/s)	$\Gamma_{L/R}$ (mm/s)	area (%)
one component	conventional annealing	0.455(5)	0.390(5)	0.34/0.32[a]	100
	arc-melting	0.477(3)	0.40(1)	0.41/0.39[a]	100
	literature, arc-melting[b]	0.42	0.41	0.40	100
two components	conventional annealing	0.53(1)	0.38(1)	0.27(2)	45(3)
		0.39(2)	0.40(1)	0.28(1)	55(3)
	arc-melting	0.53(3)	0.46(1)	0.30(2)	40(5)
		0.42(1)	0.29(2)	0.35(5)	60(5)

[a]Gaussian line shape. [b]The actual values were not included in the text. These numbers were obtained by digitizing Figure 5 of the original article.[13]

$CuFe_2Ge_2$ of only one such doublet at 200 K is puzzling, as it suggests that the electronic structures of the octahedral and trigonal-bipyramidal Fe sites are nearly indistinguishable from one another. We note that similar spectra were observed by Canfield and Bud'ko for the $CuFe_2Ge_2$ sample obtained by arc-melting.[13] Our reevaluation of the Mössbauer data presented here reveals that both the high- and low-temperature spectra originate from the superposition of at least two distinct spectral components.

For the sample prepared by conventional annealing, zero-field spectra recorded below 170 K (Figure 12) are well

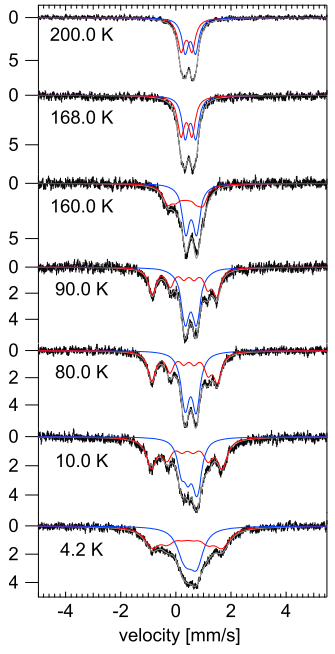

Figure 12. Temperature-dependent zero-field ^{57}Fe Mössbauer spectra recorded for the $CuFe_2Ge_2$ sample obtained by conventional annealing.

described by the overlap of two spectral components, one of which exhibits a spontaneous magnetic hyperfine splitting and the other is a quadrupole doublet. These spectra suggest that only a fraction of the Fe sites experience magnetic ordering. Specifically, lowering the temperature from 168 to 160 K leads to a dramatic increase in the hyperfine splitting of the magnetic component, followed by a more gradual development, such that the maximum hyperfine splitting observed at 4.2 K corresponds to an internal field of 7.95 T (the red curve in Figure 13). Fitting the temperature dependence of the internal field as the order parameter leads to $T_N \sim 167$ K, in good agreement with the magnetic data (Table 1 and Figure 6).

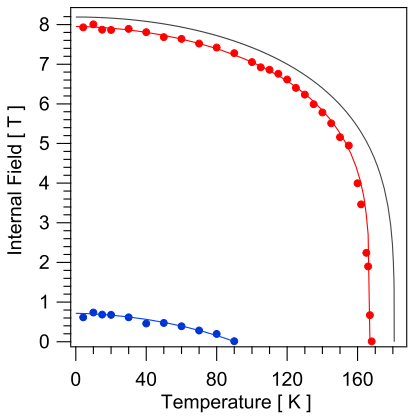

Figure 13. Temperature dependence of the internal fields observed for the major (red) and minor (blue) components of the ^{57}Fe Mössbauer spectra recorded for the $CuFe_2Ge_2$ sample prepared by conventional annealing. Shown in black is the dependence observed for the major component of the arc-melted sample in ref 13. The red and blue solid line traces are theoretical curves obtained using eq S1 and the parameters listed in Table S2. The internal field of the minor component was obtained assuming an EFG component along the internal field, $\varepsilon = -0.38(2)$ mm/s.

Interestingly, this behavior also allowed us to deconvolute the quadrupole doublets observed at higher temperatures into two spectral components (Table 2). Varying the temperature between 150 and 180 K leaves the quadrupole doublet of the paramagnetic fraction unchanged. Furthermore, its contribution to the difference spectrum taken between the spectra obtained at temperatures above and below 167 K is canceled (Figure S7). Therefore, the difference spectrum allows us to isolate the contribution of the magnetic component and derive the parameters of the corresponding quadrupole doublet above the ordering temperature. The same procedure was applied to simulate the spectra of the sample obtained by arc-melting (Figure S8), and the corresponding spectral parameters are listed in Table 2.

The recent report on $CuFe_2Ge_2$[13] revealed that the low-temperature, zero-field Mössbauer spectra of this compound are well simulated by the superposition of a sextet and a doublet, suggesting a mixture of a magnetically ordered phase and a paramagnetic phase. Nevertheless, the doublet component observed by Bud'ko *et al.* is unusually broad at 4.2 K, with a line width $\Gamma \approx 0.55$ mm/s, which is sizably larger than $\Gamma \approx 0.38$ mm/s observed above 20 K. Interestingly, we observe an analogous behavior for the sample obtained by conventional annealing (Figure 12). Below 90 K, the apparent line width of the paramagnetic component increases with lowering the temperature. Although the appearance of this spectral component at 4.2 K is reminiscent of a doublet, we

https://doi.org/10.1021/acs.inorgchem.1c02997
Inorg. Chem. 2022, 61, 4257−4269

find that the low-temperature spectra are best described by considering a relatively small magnetic hyperfine splitting induced by the internal field between 0.7 and 2.1 T. The relatively large range of values is explained by the small magnitude of the magnetic hyperfine splitting for the minor component. This feature leads to experimental spectra that lack enough resolution to determine the individual contributions of both the quadrupolar and Zeeman interactions (Figure S9a). In this case, without prior knowledge of the magnitude of the internal field (B_{int}) or the EFG along the internal field (ε), only a range of possible values and a correlation between B_{int} and ε can be derived (Figure S9b). Regardless, this analysis indicates that all Fe sites exhibit magnetic ordering, with the first ordering taking place at ∼167 K and the second ordering below 90 K, as evidenced by the evolution of the internal fields determined for the two spectral components (the red and blue traces, respectively, in Figure 13). This figure also includes the previously reported dependence determined for the magnetic component of a sample prepared by arc melting (the black trace).[13] Comparison of these traces shows that, except for some minor differences, the samples produced by the two methods exhibit a similar behavior. The observation that the Fe sites of both types exhibit magnetic ordering is further corroborated by the analysis of the field-dependent Mössbauer spectra and neutron powder diffraction (NPD) data (*vide infra*).

One notable feature of the zero-field spectra recorded for the sample prepared by conventional annealing is that the spectrum obtained at 4.2 K is considerably broader than the one recorded at 10 K (Figure 12), indicating the increase in the HFD at 4.2 K. Our simulations suggest that the dz value, describing the FWHM of the Gaussian HFD, increases by ∼70% when the temperature is lowered from 10 to 4.2 K. Interestingly, this increase is concomitant with the onset of incommensurate AFM ordering as determined from the neutron diffraction data, suggesting that the increased heterogeneity of the hyperfine fields is related to the spin density wave associated with the incommensurate AFM structure.

Field-Dependent Measurements. To investigate further the magnetic ordering in $CuFe_2Ge_2$, we recorded a series of field-dependent Mössbauer spectra (Figures 14a and S10). Our analysis suggests that both Fe sites in $CuFe_2Ge_2$ exhibit magnetic ordering. We observe that the effective hyperfine fields associated with both spectral components increase linearly with the applied field (Figure 14b,c). This observation also corroborates the presence of a non-zero internal field for the broad doublet observed in the zero-field spectrum at 4.2 K. Moreover, our simulations suggest that the 3:2:1:1:2:3 pattern of the intrinsic resonance intensities is maintained regardless of the strength of the applied field, which indicates that these species are magnetically uniaxial and that no metamagnetic transition takes place.

Albeit the zero-field spectra of $CuFe_2Ge_2$ could be well reproduced considering only two distinct spectral components, the high-field spectra could not be properly simulated in the same fashion. Using only two components to simulate the high-field spectra observed at 4−8 T accounted, at best, for only 2/3 of the total spectral area. A complete account of all Fe sites present in these samples required us to consider three distinct spectral components for the samples prepared by both synthetic methods (Figures 14a and S11). While two of these components are easily identifiable with the dominant spectral

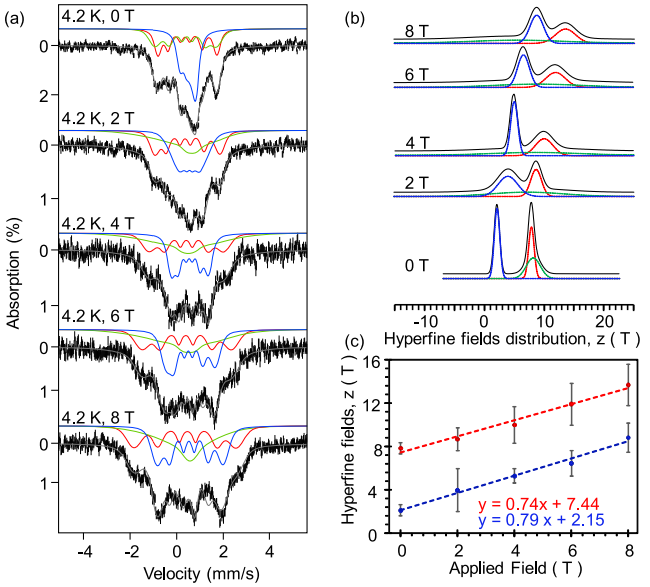

Figure 14. (a) Field-dependent ^{57}Fe Mössbauer spectra recorded for the arc-melted sample of $CuFe_2Ge_2$ at 4.2 K. The solid gray lines are simulations obtained from the sum of three components, which are individually drawn. (b) Gaussian HFDs determined from the simulation of the field-dependent spectra recorded at 4.2 K. The HFDs of individual spectral components are shown as dotted lines. (c) HFD centroids (z) of the FM-ordered components (red and blue) as a function of the applied magnetic field. The error bars are equal to dz, the FWHM of the Gaussian HFD.

features and correlate with the two components used to simulate the zero-field spectra, the third is characterized by a very broad distribution of hyperfine fields (Figure 14b). Since the low-field spectra can be equally well represented with either two or three components, Mössbauer data alone do not allow us to determine whether the presence of a third component is intrinsic to $CuFe_2Ge_2$ or if it originates from a dramatic, field-induced increase in spin disorder for a large fraction of the Fe sites associated with the major component of the zero-field spectra. While this analysis does not illuminate the magnetic ordering observed in zero-field, it does reveal that the Fe1 and Fe2 magnetic moments exhibit a parallel alignment under applied field above 2 T (Table 3). This finding agrees with the field-induced suppression of the AFM order in $CuFe_2Ge_2$ reported by May *et al.*[12]

Neutron Powder Diffraction. The differences in magnetic properties between the two synthetic methods suggest that the new synthetic route may affect the material's magnetic structure. To probe this possibility, $CuFe_2Ge_2$ prepared by conventional high-temperature annealing (without arc-melting) was studied by NPD. The NPD patterns were collected above and below T_N, as predetermined by the temperature-dependent magnetic data (Figure 6). As can be seen from the fragment of the NPD patterns shown in Figure 15, lowering the temperature below T_N results in the appearance of additional peaks due to AFM ordering. At 150, 125, and 100 K, these peaks were successfully indexed with a propagation vector $\boldsymbol{k}_1 = (0, 1/2, 0)$. Lowering the temperature to 4 K led to the change in the propagation vector, which became incommensurate, $\boldsymbol{k}_2 = (0, 1/2, \xi)$. For the lowest measured temperature of 4 K, we found $\xi = 0.087(1)$, which is slightly different from the value of 0.117 reported for the material synthesized by arc-melting.[12] Furthermore, contrary to the

https://doi.org/10.1021/acs.inorgchem.1c02997
Inorg. Chem. 2022, 61, 4257−4269

Table 3. Hyperfine Splitting Parameters Used to Describe the FM Components of the Zero-Field, 4.2 K Spectra of the $CuFe_2Ge_2$ Sample Obtained by Arc-Melting[a]

model	Γ, mm/s	δ, mm/s	ε, mm/s	z, T	dz, T	area, %	reference
2-FM	0.27	0.43	0.03	7.8	2.0	59(5)	this work
	0.27	0.55	−0.51	1.0	1.0	40(5)	
3-FM	0.27	0.43	0.10	7.8	1.0	30(5)	
	0.27	0.43	−0.19	8.1	2.7	30(5)	
	0.27	0.55	−0.13	2.11	1.1	40(7)	
1-FM	0.41	0.55[b]	−0.08[b]	8.2[c]		60[b]	13

[a]The 1-FM, 2-FM, and 3-FM labels refer to the models that considered one, two, or three different components characterized by non-zero magnetic hyperfine splitting parameters, z and dz. [b]The actual values were not given in the literature. They were obtained by digitizing Figure 5 of the original article. [c]The actual value was not given in the literature. Rather, it was obtained using the expression $B_{hf}(T) = 8.19(1 - (T/180.8)^{2.0})^{0.27}$ and $T = 4.2$ K.

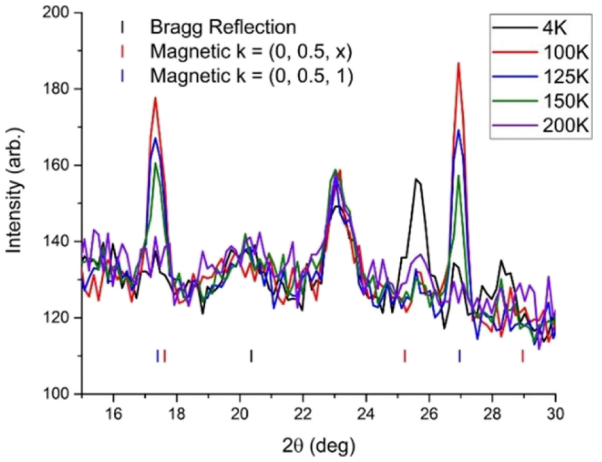

Figure 15. Selected fragment of temperature-dependent NPD pattern recorded for the sample of $CuFe_2Ge_2$ prepared by conventional annealing.

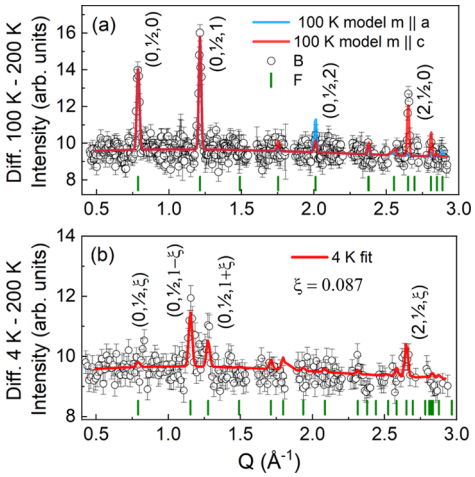

Figure 16. Magnetic scattering at 100 (a) and 4 K (b) obtained by subtracting the nuclear contribution measured at 200 K. The fits to magnetic structure models are shown by solid lines. Comparisons of the fitting results in (a) demonstrates that the moments are mainly aligned along the c-axis. The best fit of the 4 K scattering in (b) accounts for the different intensities of the satellite reflections (0, 1/2, and 1 ± 0.087), which indicates that the modulations of the Fe2 moments at the vertices of the saw-tooth chain are offset by a phase shift.

report by May *et al.*, who observed an onset of the incommensurate spin density wave at 125 K and the co-existence of the commensurate and incommensurate magnetic structures between 125 and 100 K, we observe only a commensurate magnetic structure at both 125 and 100 K. The diffraction pattern collected at 4 K for the sample obtained by conventional annealing displays only the incommensurate magnetic peaks. These difference from the earlier work, which used NPD data recorded on arc-melted samples, yet again highlight the process-dependent changes in the magnetic behavior of the $CuFe_2Ge_2$ samples.

Rietveld refinements of the commensurate and incommensurate magnetic structures were carried out using the difference data, [100 − 200 K] and [4 − 200 K], respectively, to decouple the magnetic structure from the nuclear structure refinement. Such a procedure was necessitated by the weak intensity of the magnetic peaks, which were smaller than 1% of the strongest nuclear Bragg peaks. The data points around the strong nuclear peaks whose positions were affected by temperature-induced changes in lattice parameters have been excluded. The magnetic scattering isolated in such a way and the best fits to the data are showed in Figure 16. The magnetic scattering at 100 K is well reproduced using the magnetic structure model proposed by May *et al.*[12] The Fe1 spins form FM chains along the a-axis and are coupled AFM to the nearest-neighbor Fe2 spins (Figure 10). The magnetic chains compensate each other by alternating their spin direction along the b-axis (Figure S13a). Previous report also pointed out that two models, with moments pointing along either a- or c-axis, describe the data equally well, but the model with spins parallel to the c-axis was preferred based on the results of first-principles calculations. The analysis of our NPD data clearly demonstrates that the moments are parallel to the c-axis. This is evidenced by a much stronger intensity of the (2, 1/2, 0) magnetic peak as compared to the intensity of the (0, 1/2, 2) peak (Figure 16a). The magnetic structure is described by the magnetic space group P_cbcm (#57.388) in the magnetic unit lattice base (a, $2b$, and c). In this symmetry, the Fe1 moments are confined to the ac plane, while the Fe2 moments are constrained along the c-axis. Further details of the spin model are given in the Supporting Information. The moments refined from the 100 K NPD pattern were 1.5(1) μ_B for Fe1 and 0.5(1) μ_B for Fe2.

The analysis of the incommensurate magnetic scattering observed at 4 K reveals that the spins preserve their orientations along the c-axis but oscillate in magnitude to from a longitudinal spin-density wave (Figure S13b), defined by the incommensurate wave vector $\boldsymbol{k}_2$ = (0, 1/2, and 0.087). This magnetic structure is described by a (3 + 1)-dimensional magnetic superspace group $Pmma1'(0, 1/2, g)s00s$, which

https://doi.org/10.1021/acs.inorgchem.1c02997
Inorg. Chem. 2022, 61, 4257−4269

includes the standard symbol of a gray Shubnikov group, *Pmma*1′, followed by the propagation vector, where *g* denotes the irrational component of ***k***, and an intrinsic translation (*s*00*s*) associated with the point-group generator.[33] The only difference of our model from the one proposed previously[12] consists in the presence of a phase shift between the modulations of the Fe2 moment at the vertices of the saw-tooth chain (*i.e.*, $m_2' = m_2 \cdot e^{-2\pi\varphi}$). This phase shift accounts for the non-equal intensities of the satellite reflections, (0, 1/2, and 1 ± 0.087), depicted in Figure 16b. The moments refined at 4 K are 1.3(1) μ_B for Fe1 and 1.0(1) μ_B for Fe2, with φ = 0.07(5). These values are slightly larger than those reported by May *et al.*, but closer to the values estimated by the DFT calculations in the same work (1.25 μ_B for Fe1 and 0.90 μ_B for Fe2).

CONCLUSIONS

The series of solid solutions $CuFe_{2-x}Co_xGe_2$ exhibits gradual suppression of magnetic ordering with the increase in the d-electron concentration. While the population of the 3d sub-band is sufficient to cause itinerant antiferromagnetism in $CuFe_2Ge_2$, the substitution of Co for Fe leads to the suppression of AFM ordering and rapid decrease in the T_N value, with the spin-glass behavior observed in $CuFeCoGe_2$. The crystal orbital Hamilton population (COHP) analysis of bonding between Fe/Co atoms explains these observations in terms of the transition from strongly antibonding to non-bonding interactions and a strong decrease in the DOS at the Fermi level upon increase in the d-electron count. Probing the magnetic ordering by Mössbauer spectroscopy reveals a remarkably insightful correlation with the COHP analysis, as both strongly and weakly ordered magnetic components are observed. The component with the smaller hyperfine splitting parameter, most likely, reflects the presence of competing magnetic interactions at the Fe(2) site. The study of the field-dependent Mössbauer spectra clearly shows that the spectral component with the smaller hyperfine splitting also corresponds to magnetically ordered sites and not to a paramagnetic phase. Moreover, the results of magnetic measurements, Mössbauer spectroscopy, and neutron diffraction studies on the $CuFe_2Ge_2$ sample prepared by two different methods, arc-melting or conventional annealing, consistently suggest that the magnetic behavior of this material is dependent on the thermal processing conditions. In particular, the sample prepared by conventional annealing showed clear separation between the commensurate and incommensurate magnetic structures as a function of temperature, while a co-existence of both magnetic structures over a certain temperature range was previously reported for an arc-melted sample. These observations agree with the higher heterogeneity of magnetic parameters in the arc-melted samples, as established by Mössbauer spectroscopy.

Finally, we would like to point out that the observation of the strong peak in the DOS of $CuFe_2Ge_2$ immediately below the Fermi level raises the question of whether the decrease in the d-electron concentration might lead to a more robust ferromagnetic behavior. These studies are currently under way in our laboratories, and their results will be reported in due course.

ASSOCIATED CONTENT

Supporting Information

The Supporting Information is available free of charge at https://pubs.acs.org/doi/10.1021/acs.inorgchem.1c02997.

Plots of temperature-dependent PXRD patterns and unit cell parameters, field-dependent magnetization data, additional Mössbauer data, and magnetic structures of $CuFe_2Ge_2$ (PDF)

AUTHOR INFORMATION

Corresponding Authors

Sebastian A. Stoian − *Department of Chemistry, University of Idaho, Moscow, Idaho 83844, United States;* orcid.org/0000-0003-3362-7697; Email: sstoian@uidaho.edu

Michael Shatruk − *Department of Chemistry and Biochemistry, Florida State University, Tallahassee, Florida 32306, United States; National High Magnetic Field Laboratory, Tallahassee, Florida 32310, United States;* orcid.org/0000-0002-2883-4694; Email: mshatruk@fsu.edu

Authors

Zachary P. Tener − *Department of Chemistry and Biochemistry, Florida State University, Tallahassee, Florida 32306, United States;* Present Address: Neutron Scattering Division, Oak Ridge National Laboratory, Oak Ridge, TN 37831, United States

Vincent Yannello − *Department of Chemistry and Biochemistry, Florida State University, Tallahassee, Florida 32306, United States;* Present Address: Department of Chemistry, Biochemistry and Physics, University of Tampa, Tampa, FL 33606, United States

V. Ovidiu Garlea − *Neutron Scattering Division, Oak Ridge National Laboratory, Oak Ridge, Tennessee 37831, United States*

Saul H. Lapidus − *X-ray Science Division, Argonne National Laboratory, Lemont, Illinois 60439, United States*

Philip Yox − *Department of Chemistry, Iowa State University, Ames, Iowa 50011, United States; Ames Laboratory, United States Department of Energy, Ames, Iowa 50011, United States;* orcid.org/0000-0002-8524-8202

Kirill Kovnir − *Department of Chemistry, Iowa State University, Ames, Iowa 50011, United States; Ames Laboratory, United States Department of Energy, Ames, Iowa 50011, United States*

Complete contact information is available at: https://pubs.acs.org/10.1021/acs.inorgchem.1c02997

Notes

The authors declare no competing financial interest.

ACKNOWLEDGMENTS

This research was supported by the National Science Foundation (award DMR-1905499). Part of this work was performed at the National High Magnetic Laboratory (NHMFL), which is supported by the NSF (award DMR-1644779) and the State of Florida. S.A.S. would also like to acknowledge the support of the University of Idaho. The Mössbauer instrument was purchased using the NHFML User Collaboration Grant Program (UCGP-5064) awarded to Dr. Andrzej Ozarowski. The variable-temperature studies performed by P.Y. and K.K. were supported by the Laboratory

Research and Development Program of the Ames Laboratory under the U.S. Department of Energy contract no. DE-AC02-07CH11358. This research used resources of the Advanced Photon Source (APS), a U.S. Department of Energy (DOE) Office of Science User Facility operated for the DOE Office of Science by Argonne National Laboratory (ANL) under contract no. DE-AC02-06CH11357. We thank Dr. W. Xu and Dr. A. Yakovenko for help with conducting the *in situ* PXRD measurements at 17-BM (APS-ANL). A portion of this research used resources at the High Flux Isotope Reactor, a DOE Office of Science User Facility operated by the Oak Ridge National Laboratory.

REFERENCES

(1) Takahashi, H.; Igawa, K.; Arii, K.; Kamihara, Y.; Hirano, M.; Hosono, H. Superconductivity at 43 K in an iron-based layered compound LaO1-xFxFeAs. *Nature* **2008**, *453*, 376−378.
(2) Hosono, H. Layered Iron Pnictide Superconductors: discovery and current status. *J. Phys. Soc. Jpn.* **2008**, *77*, 1−8.
(3) Rotter, M.; Pangerl, M.; Tegel, M.; Johrendt, D. Superconductivity and crystal structures of $(Ba_{1-x}K_x)Fe_2As_2$ (x = 0-1). *Angew. Chem., Int. Ed.* **2008**, *47*, 7949−7952.
(4) Rotter, M.; Tegel, M.; Johrendt, D. Superconductivity at 38 K in the Iron Arsenide (Ba1-xKx)Fe2As2. *Phys. Rev. Lett.* **2008**, *101*, 107006.
(5) Canfield, P. C.; Bud'ko, S. L. FeAs-based superconductivity: a case study of the effects of transition metal doping on $BaFe_2As_2$. *Annu. Rev. Condens. Matter Phys.* **2010**, *1*, 27−50.
(6) Mizuguchi, Y.; Demura, S.; Deguchi, K.; Takano, Y.; Fujihisa, H.; Gotoh, Y.; Izawa, H.; Miura, O. Superconductivity in novel BiS_2-based layered superconductor $LaO_{1-x}F_xBiS_2$. *J. Phys. Soc. Jpn.* **2012**, *81*, 114725.
(7) Mizoguchi, H.; Kuroda, T.; Kamiya, T.; Hosono, H. $LaCo_2B_2$. A Co-based layered superconductor with a $ThCr_2Si_2$-type structure. *Phys. Rev. Lett.* **2011**, *106*, 237001.
(8) Chen, J.; Semeniuk, K.; Feng, Z.; Reiss, P.; Brown, P.; Zou, Y.; Logg, P. W.; Lampronti, G. I.; Grosche, F. M. Unconventional superconductivity in the layered iron germanide YFe_2Ge_2. *Phys. Rev. Lett.* **2016**, *116*, 127001.
(9) Wu, G.; Xie, Y. L.; Chen, H.; Zhong, M.; Liu, R. H.; Shi, B. C.; Li, Q. J.; Wang, X. F.; Wu, T.; Yan, Y. J.; Ying, J. J.; Chen, X. H. Superconductivity at 56 K in samarium-doped SrFeAsF. *J. Phys.: Condens. Matter* **2009**, *21*, 142203.
(10) Wang, C.; Li, L.; Chi, S.; Zhu, Z.; Ren, Z.; Li, Y.; Wang, Y.; Lin, X.; Luo, Y.; Jiang, S.; Xu, X.; Cao, G.; Xu, Z. A. Thorium-doping-induced superconductivity up to 56 K in $Gd_{1-x}Th_xFeAsO$. *Europhys. Lett.* **2008**, *83*, 67006.
(11) Shanavas, K. V.; Singh, D. J. Itinerant magnetism in metallic $CuFe_2Ge_2$. *PLoS One* **2015**, *10*, No. e0121186.
(12) May, A. F.; Calder, S.; Parker, D. S.; Sales, B. C.; McGuire, M. A. Competing magnetic ground states and their coupling to the crystal lattice in $CuFe_2Ge_2$. *Sci. Rep.* **2016**, *6*, 35325.
(13) Bud'ko, S. L.; Jo, N. H.; Downing, S. S.; Canfield, P. C. On magnetic structure of $CuFe_2Ge_2$: constrains from the ^{57}Fe Mössbauer spectroscopy. *J. Magn. Magn. Mater.* **2018**, *446*, 260−263.
(14) Landrum, G. A.; Dronskowski, R. Ferromagnetism in transition metals: a chemical bonding approach. *Angew. Chem., Int. Ed.* **1999**, *38*, 1389−1393.
(15) Landrum, G. A.; Dronskowski, R. The orbital origins of magnetism: from atoms to molecules to ferromagnetic alloys. *Angew. Chem., Int. Ed.* **2000**, *39*, 1560−1585.
(16) Dronskowski, R.; Bloechl, P. E. Crystal Orbital Hamilton Populations (COHP)—energy-resolved visualization of chemical bonding in solids based on density-functional calculations. *J. Phys. Chem.* **1993**, *97*, 8617−8624.
(17) Shatruk, M. Chemical aspects of itinerant magnetism. In *Encyclopedia of Inorganic and Bioinorganic Chemistry*; Scott, R. A., Ed.; Wiley-VCH: Chichester, 2017.
(18) Tan, X.; Tener, Z. P.; Shatruk, M. Correlating itinerant magnetism in RCo_2Pn_2 pnictides (R = La, Ce, Pr, Nd, Eu, Ca; Pn = P, As) to their crystal and electronic structures. *Acc. Chem. Res.* **2018**, *51*, 230−239.
(19) Zavalij, I. Y.; Pecharsky, V. K.; Bodak, O. I. Crystal structures of $CuFe_2Ge_2$ and $Cu_{1+/-x}Co_{2-/+x}Ge_2$. *Kristallografiya* **1987**, *32*, 66−69.
(20) *X'Pert HighScore Plus Software V. 2.2b*; PANalytical B.V.: Almelo, Netherlands, 2006.
(21) Rodríguez-Carvajal, J. Recent advances in magnetic-structure determination by neutron powder diffraction. *Phys. B* **1993**, *192*, 55−69.
(22) Chupas, P. J.; Chapman, K. W.; Kurtz, C.; Hanson, J. C.; Lee, P. L.; Grey, C. P. A versatile sample-environment cell for non-ambient X-ray scattering experiments. *J. Appl. Crystallogr.* **2008**, *41*, 822−824.
(23) Rancourt, D. G.; Ping, J. Y. Voigt-based methods for arbitrary-shape static hyperfine parameter distributions in Mössbauer spectroscopy. *Nucl. Instrum. Methods Phys. Res., Sect. B* **1991**, *58*, 85−97.
(24) Wills, A. S. A new protocol for the determination of magnetic structures using simulated annealing and representational analysis (SARAh). *Phys. B* **2000**, *276*−*278*, 680−681.
(25) Perez-Mato, J. M.; Gallego, S. V.; Tasci, E. S.; Elcoro, L.; de la Flor, G.; Aroyo, M. I. Symmetry-based computational tools for magnetic crystallography. *Annu. Rev. Mater. Res.* **2015**, *45*, 217−248.
(26) Tank, R.; Jepsen, O.; Burkhardt, A.; Andersen, O. K. *The Program TB-LMTO-ASA*, Version 4.7; Max-Planck-Institut fur Festkorperforschung: Stuttgart, 1999.
(27) von Barth, U.; Hedin, L. Local exchange-correlation potential for the spin-polarized case I. *J. Phys. C: Solid State Phys.* **1972**, *5*, 1629−1642.
(28) Lambrecht, W. R. L.; Andersen, O. K. Minimal basis sets in the linear muffin-tin orbital method: application to the diamond-structure crystals carbon, silicon, and germanium. *Phys. Rev. B: Condens. Matter Mater. Phys.* **1986**, *34*, 2439−2449.
(29) Löwdin, P. O. A Note on the Quantum-Mechanical Perturbation Theory. *J. Chem. Phys.* **1951**, *19*, 1396−1401.
(30) Mydosh, J. A. *Spin Glasses: An Experimental Introduction*; Taylor & Francis: Washington, DC, 1993.
(31) Stoner, E. C. Collective electron ferromagnetism. *Proc. R. Soc. London, Ser. A* **1938**, *165*, 372−414.
(32) Janak, J. F. Uniform susceptibilities of metallic elements. *Phys. Rev. B: Solid State* **1977**, *16*, 255−262.
(33) Perez-Mato, J. M.; Ribeiro, J. L.; Petricek, V.; Aroyo, M. I. Magnetic superspace groups and symmetry constraints in incommensurate magnetic phases. *J. Phys.: Condens. Matter* **2012**, *24*, 163201.

https://doi.org/10.1021/acs.inorgchem.1c02997
Inorg. Chem. 2022, 61, 4257−4269